**ORIGINAL ARTICLE**

**Near Surface Geophysics** | EAGE EUROPEAN ASSOCIATION OF GEOSCIENTISTS & ENGINEERS

# GPR modelling and inversion to quantify the debris content within ice

**Ilaria Santin** ⓘ | **Giacomo Roncoroni** ⓘ | **Emanuele Forte** ⓘ | **Pietro Gutgesell** | **Michele Pipan** ⓘ

Department of Mathematics and Geosciences, University of Trieste, Trieste, Italy

**Correspondence**
Santin Ilaria, Department of Mathematics and Geosciences, University of Trieste, via Weiss, 2, 34128 Trieste, Italy. Email: ilaria.santin@phd.units.it

**Abstract**

Scattering is often detected when ground-penetrating radar (GPR) surveys are performed on glaciers at different latitudes and in various environments. This event is often seen as an undesirable feature on data, but it can be exploited to quantify the debris content in mountain glaciers through a dedicated scattering inversion approach. At first, we considered the possible variables affecting the scattering mechanisms, namely the dielectric properties of the scatterers, their size, shape and quantity, as well as the wavelength of the electromagnetic (EM) incident field to define the initial conditions for the inversion. Each parameter was independently evaluated with forward modelling tests to quantify its effect in the scattering mechanism. After extensive tests, we found that the dimension and the amount of scatterers are the crucial parameters. We further performed modelling randomizing the scatterer distribution and dimension, critically evaluating the stability of the approach and the complexity of the models. After the tests on synthetic data, the inversion procedure was applied to field datasets, acquired on the Eastern Gran Zebrù glacier (Central Italian Alps). The results show that even a low percentage of debris can produce high scattering. The proposed methodology is quite robust and able to provide quantitative estimates of the debris content within mountain glaciers in different conditions.

**KEYWORDS**
dielectric properties, ground-penetrating radar, heterogeneity, inversion, modelling

## INTRODUCTION

Retrieving quantitative information about subsurface targets from ground-penetrating radar (GPR) data can be a challenging task, particularly when the signal-to-noise ratio is low. Automatic analyses based on statistical approaches (see, e.g., Roncoroni et al., 2022) are not frequently applied to GPR data interpretation. The role of GPR modelling is essential in advancing the GPR interpretation as it can provide additional information on targets by accurately reproducing the response of subsurface materials to electromagnetic (EM) waves. By simulating the propagation of these waves through different types of subsurface materials with various geometries, numerical modelling can reproduce how EM waves interact with the expected subsurface features, such as buried objects (Diamanti & Annan, 2019; González-Huici & Giovanneschi, 2013; Kelly et al., 2021), geological structures (Giannopoulos & Diamanti, 2008; Öztürk & Drahor, 2010), water content variations (Bano, 2006), as well as a glaciers' internal structure (Hunziker et al., 2023; Moran et al., 2003). This information can further be used to discriminate between real subsurface features and coherent noise or artefacts that can hinder interpretation. Additionally, numerical modelling can help survey design

optimization by predicting the expected GPR signal response in different scenarios and by identifying potential sources of interference (Diamanti et al., 2022). Overall, GPR forward modelling is a powerful tool that can enhance the accuracy and reliability of GPR data interpretation, providing valuable insights into the subsurface features of interest. In this research, we propose an application of numerical GPR forward modelling and scattering inversion to get quantitative information on the debris content in glaciers, focusing on the high scattering zone (HSZ) sometimes imaged within GPR glaciological surveys. In a GPR profile, an EM transparent facies is a typical marker for clean ice (i.e., without impurities due to water or debris), but scattering phenomena are quite common within glaciers. According to the basic EM theory (see, e.g., Tsang et al., 2000), scattering phenomena occur when a propagating EM wave interacts with a particle having dielectric properties different from its surroundings; it continuously removes energy from the EM wavefield by diffracting it in all directions. If the particle size is smaller than or comparable to the wavelength of the incident wave, the phenomenon is well described by the Rayleigh (1881) and Mie (1908) scattering theories, respectively. The number of scattering events and their energy depend on several factors, including the dielectric properties of the scatterers, in addition to their dimensions and amount, the wavelengths and the radiation pattern of the EM incident field. Scattering phenomena affect the EM wave amplitude, lowering it by a coefficient of scattering depending on the amount of scatterers and their cross-section versus the wavelength of the incident EM wave. Therefore, the frequency used in GPR surveys has a crucial role in the scattering level and its characteristics (Jol, 2009). According to the Rayleigh criterion, particles with a dimension smaller than the wavelength produce scattering phenomena, whereas particles larger than the wavelength will produce clear reflections (except at the borders where diffractions are also produced). Naval et al. (2018) proposed an empirical threshold of one eighth of the wavelength corresponding to the dominant frequency of the GPR signal as the minimum dimension of scatterers, below which there are almost no reflections or diffractions.

Scattering events in GPR profiles on glaciers can be attributable to three main different glaciological settings: (1) isolated debris particles or boulders within the ice generating single diffractions hyperbolas; (2) crevasses, moulins and other glaciological features producing a set of high dipping aligned scattering events, crossing most of the ice thickness; (3) a diffuse scattering facies (referred hereafter as HSZ) often imaged within GPR profiles and usually interpreted as diagnostic for liquid water (e.g., Delf et al., 2022). Indeed, such HSZ can be, therefore, related to warm ice, the temperature of which not only allows the occurrence of liquid water (e.g., Pet-

tersson et al., 2007; Reinardy et al., 2019) but also to mixtures of ice and debris (e.g., Colombero et al., 2019; King et al., 2008).

The proposed methodology starts from the work presented in Forte et al. (2021) and Santin et al. (2022) that focused on assessing the physical meaning of an HSZ imaged in the Eastern Gran Zebrù glacier GPR dataset, specifically in terms of debris content and characteristics. In particular, we focused on a 250-MHz ground-based survey collected in 2019 with a ProEx (MALÅ Geoscience) GPR system, encompassing a total of 6.1-km GPR profiles. The processing flow includes drift removal, bandpass filtering, background removal, exponential amplitude recovery and depth conversion. The primary purpose of the processing is to increase the signal/noise ratio maintaining the original data signature and, in particular, not distorting the shape/amplitude of diffractions which are used as input of the proposed inversion procedure. For this reason, we obviously did not apply any migration algorithm. For further details about data acquisition, processing and interpretation, please refer to Forte et al. (2021). Forte et al. (2021) managed to assess the physical meaning of the HSZ through a differential diagnosis approach. In fact, as in many cases, no direct information (like core samples) is available, it is essential to limit the subjectivity of the interpretation by the integration of discriminative hypotheses based on both independent and integrated criteria. In the above-cited case, differential diagnosis analysis allowed to associate the HSZ to a mixture of ice and debris, rather than to warm ice. The starting problem for this study is: as an amount of about 2% in volume of water in ice is sufficient to cause high scattering and significantly increase the intrinsic attenuation (Bradford et al., 2009), how much debris can produce such an effect and what is the signature of GPR data due to different debris contents? We present a methodology able to estimate the percentage of debris through scattering amplitude inversion. The procedure is tested first on synthetic data and then on the GPR dataset collected on the Eastern Gran Zebrù glacier (Italian Alps).

A synthetic GPR model, mimicking field data, was built to first analyse and critically evaluate the separate effect of different parameters (debris dimensions, dielectric properties, scatterer shapes and amount) in the scattering energy behaviour through dedicated synthetic simulations adopted as sensitivity tests. This preliminary assessment made it possible to simplify the subsequent inversions by focusing on just two parameters, namely the size and the volume fraction of debris. The results obtained by the differential diagnosis in Forte et al. (2021), encompassing GPR data interpretation, spectral properties and inferences from the scattering theory, contributed to the geological constraints for the inversion. Although HSZs can be the most apparent EM facies in some GPR profiles, we found that less than
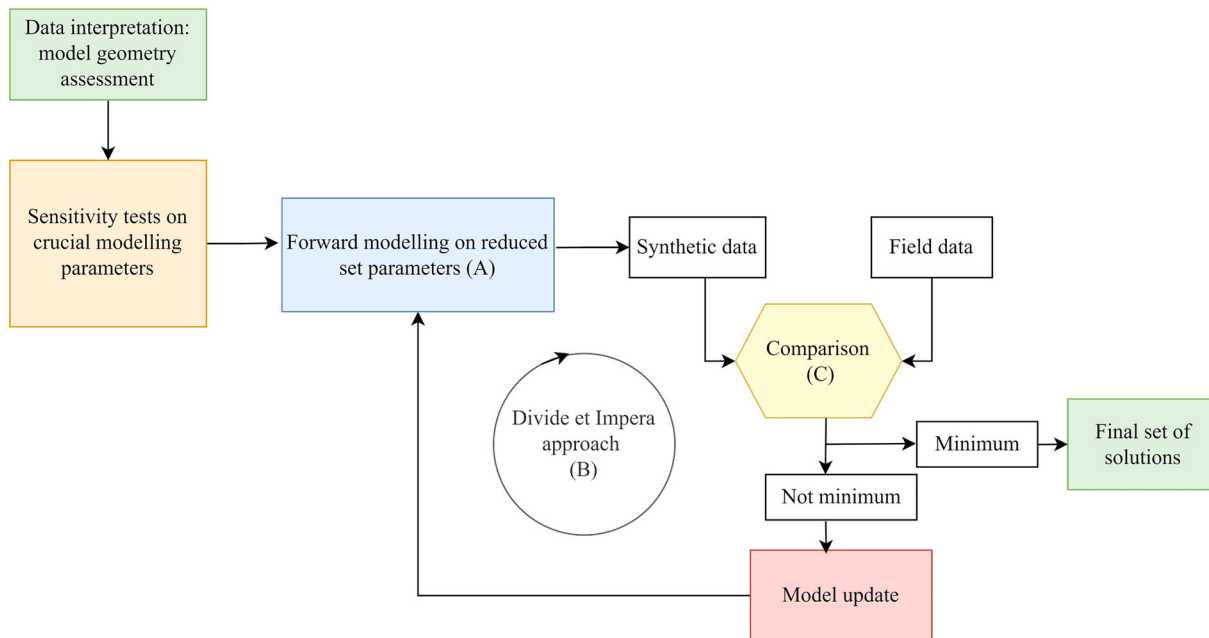
**FIGURE 1** Block diagram summarizing the proposed workflow. After a preliminary analysis of the scattering parameters, the inversion is carried out in a loop (ABC) with model parameters iteratively updated according to a *divide et impera* approach (a). The loop is based on forward modelling carried out with *gprMax* (A), and the misfit is computed between simulated and field data according to a target function (c) further described in the text (Equations 1–3).

10% of debris, randomly ranging in size, is sufficient to produce remarkable scattering.

## METHODS

We propose a methodology (Figure 1) based on an inversion procedure exploiting measured scattered amplitudes on common offset GPR datasets to estimate the debris content in ice. Prior to the inversion, we made sensitivity tests of the parameters affecting the scattering phenomenon in order to reduce the amount of model parameters in the inversion, which is based on steps A–C shown in Figure 1. We analysed the effect of the dielectric properties, geometries (in terms of shape and dimension) and the amount of scatterers as well as the wavelength of the EM incident field, on the scattering process. The results of the sensitivity tests allowed to reduce the crucial parameters for the inversion (Figure 1a–c), focusing on the amount of scatterers (i.e., the rock fraction) and their dimensions. Although the rock fraction is the main inversion parameter, the sensitivity tests allowed to narrow the range of the scatterer dimension, as further described in the discussion section. Through a class of algorithm defined as *divide et impera* (Figure 1 – step B), we aimed at reaching the minimization of a defined target function (Figure 1 – step C) which allowed to provide an estimation of the rock fraction responsible for the HSZ on the GPR field data.

Numerical simulations, both for the sensitivity tests and the forward modelling, were performed exploiting *gprMax*, version 3.1.6 (Warren et al., 2016), which is an open-source software designed to simulate the propagation of an EM wave even in heterogenous media, by solving Maxwell's equations in 3-D using the finite-difference time-domain method. The algorithm can handle complex geometries and materials distributions, being highly adaptable to model a wide range of subsurface scenarios in various fields of application, such as archaeology, civil engineering, glaciology, and hydrogeology, among others (e.g., Cheng et al., 2023; Feng et al., 2023; Haruzi et al., 2022; Hillebrand et al., 2021; Pajewski et al., 2017; Schennen et al., 2022). In order to reduce the computational costs due to model discretization, we exploited a specific module for *gprMax* modelling on GPU (Warren et al., 2018) and performed the inversion on Cineca Marconi 100 cluster with 2 CPUs with 16 cores 3.1 GHz, 4 NVIDIA Volta V100 16GB GPUs and 256 GB RAM per node running on GPUs and parallelized on several nodes.

## Forward modelling (sensitivity tests and inversion step A)

In order to evaluate the performance of our approach, we made a synthetic model mimicking a portion of a real GPR profile in which a clean ice facies, without apparent water percolation effects, lies just above the HSZ
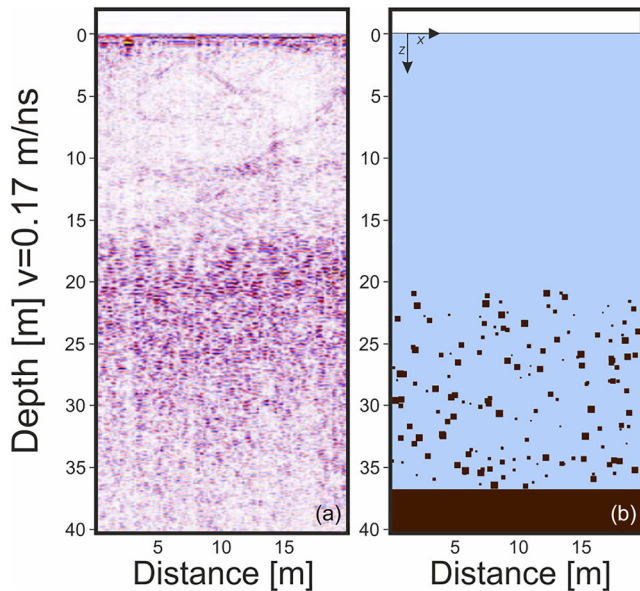
**FIGURE 2** (a) Real data and (b) three-layer model set for numerical simulation: clean ice layer (top – light blue), zone with a random distribution of scatterers with random dimension (middle) and bedrock (bottom). As both the scatterers and the bedrock have all the same relative electrical permittivity, they are both in brown (see text for further details).

(Figure 2), taken from the GPR dataset described in Forte et al. (2021). The GPR transparent facies results in low attenuation and dispersion, thus making the simulation easier to perform. The HSZ was defined from field data in time [ns], considering three surfaces (topographic surface, top of HSZ and HSZ-bedrock boundary) and converted in depth [m] using 0.17 m/ns EM constant velocity, just for an easier qualitative visual comparison between field data and synthetic model (Figure 2a,b, respectively). In the field GPR data, the HSZ-bedrock boundary was not always recognizable due to scattering and the discontinuous low-amplitude trend of the reflector; therefore, it was interpreted by exploiting GPR attributes analysis and cross-validating its location in the entire GPR dataset (Forte et al., 2021). The model is composed of three parallel layers, from top to bottom: clean ice, HSZ and bedrock, respectively (Figure 2b). Clean ice is characterized by a relative dielectric permittivity of 3.2 (Evans, 1965), whereas for scatterers and bedrock, it was set to 7.0. The electrical conductivity was set equal to zero for both ice and debris. The scatterers are characterized by a square shape with a uniform distribution of dimensions within a selected range (see the 'RESULTS AND DISCUSSION' section for further explanation). The model domain is 20 m × 40 m (in $x$ and $z$ dimensions) as shown in Figure 2b, with a cell size equal to 0.01 m. Such a small discretization of the model is essential not only for numerical stability but, even more importantly, to properly resemble small scatterers. We

set the default behaviour for the absorbing boundary conditions as the first-order complex frequency shifted perfectly matched layers, composed of 10 cells for each side of the cell domain. Therefore, we run 2-D simulations considering parallel layers with a 1-D velocity model, equal to 0.17 m/ns, with a record length equal to the recording time of field data. We considered scatterer distribution randomly generated at each new simulation to randomize synthetic data. This choice allows us to generate a complex scenario with unknown spatial distribution of debris, without falling into specific model features; for example, we can randomly generate a big cluster of several small debris particles that would globally produce scattering. To make comparable synthetic and real data, we used in the simulation a GPR wavelet with a central frequency of 250 MHz extracted from the air wave of real data, as described in Dossi et al. (2018). The GPR source is placed on the ice surface for all the simulations. As gprMax output, we considered the electric field in $z$-direction $E_z$, being in models $E_y = 1$.

Further details of models and simulation parameters, as well as all the Python codes for the inversion, are available on the GitHub page (https://github.com/Giacomo-Roncoroni/HSZ).

## The divide et impera algorithm (step B)

The inversion is based on a class of algorithms that exploit the subdivision of a main problem in smaller sub-problems of the same kind. In particular, the combination of the solutions obtained for each sub-problem provides a general solution to the main problem (Maisto et al., 2015). The proposed approach is often referred to as *divide et impera* (a.k.a., *divide and conquer*) (Barto & Mahadevan, 2003). Regarding our inversion, we selected this approach to reduce the range of rock fraction values, excluding unrealistic results after each inversion: We first focused the search on local minima of the target function, and then, inside this subset, we aimed at reaching the global minimum. We reduced the range of rock fraction to values not greater than 50% because amounts above this threshold are unrealistic in Alpine glaciers. In addition, a rock fraction higher than 50% would cause a clear reflection at the clean ice–HSZ boundary, which does not occur in field GPR data. Starting from the 50% threshold, we have progressively decreased the rock fraction in steps of 10%. Considering that for a rock fraction close to 10%, a local minimum of the target function was observed, we iterated the inversion by reducing the rock fraction by 1% steps in each inversion.

As far as the scatterer dimensions, we at first considered scatterers with fixed dimensions and then randomized them within a specific range (in our test from 0.13 m to 0.60 m).

## Inversion: target function (step C)

The inversion is based on the minimization of a target function $T(f,s)$ dependent on both field ($f$) and synthetic ($s$) data. We defined a function, called *Trend* from now on, which considers the despiking of the mean energy of the traces. The inversion is based on the minimization of the difference between the *Trends* of field and synthetic data.

The despiking operator (depk) exploits a moving average window applied over each GPR trace (i.e., A-scan) as:

$$\text{depk}\ (\text{trace}\,(t)) = \sum_{i=1}^{t-w} \left( \frac{1}{w} \sum_{k=i}^{i+w} \text{trace}\,(k) \right), \qquad (1)$$

where $t$ is the time length of trace and $w$ is window length. We define the 'Trend' as:

$$\text{Trend}_{\text{data}} = \text{depk}\left( \sqrt{\sum_{j=1}^{n} \left( \text{trace}_j\,(t) \right)^2} \right), \qquad (2)$$

with $n$ the number of traces in data and $\text{trace}_j\,(t)$ the $j$th A-Scan. Finally, we define the target function to be minimized as:

$$T\,(f, s) = \left\lVert \text{Trend}_{\text{field}} - \text{Trend}_{\text{synthetic}} \right\rVert_2^2. \qquad (3)$$

The 'Trend' is more suitable than the scattering amplitude itself in comparing field and synthetic signals because it minimizes outliers; therefore, it was chosen to build the target function to estimate the variation of scattering amplitude as a function of time. In addition, 'Trend' introduces an essential constraint to the inversion, as it allows to evaluate the occurrence of reflection events at the interfaces. In fact, reflections between clean ice and HSZ, and HSZ and bedrock, can be caused by a combination of either large percentage–small or small percentage–large scatterers. The integration of such constraint makes the inversion procedure more robust in evaluating the real cases, as it helps in reducing the range of the parameters.

## RESULTS AND DISCUSSION

### Preliminary sensitivity tests on crucial modelling parameters

The sensitivity tests were essential to evaluate the role of each parameter in the scattering process, allowing to simplify the subsequent inversion by focusing on the most relevant ones.

In the tests, we always set constant parameters varying only one of them for each test, in addition to the scatterer dimensions. Relative electrical permittivity was set equal to 3.2 and 7.0 for ice and debris, respectively; electrical conductivity was set equal to 0.0 mS/m for both ice and debris; scatterers were randomly distributed with square shape; rock fraction was equal to 5%.

At first, we evaluated the effect of the shape and distribution of the scatterers, considering both circular or squared shapes with both fixed (e.g., a layered distribution) and totally random distributions of the scatterers. From a computational point of view, the square shape takes less computation time in numerical simulation, as circle boundary must be discretized in smaller cells to prevent the introduction of artefacts in the modelled data. In addition, squares and circles produce nearly the same amount of scattering, with less than 5% discrepancy. This difference is attributable to the discretization of circles, which increases the amount of angles causing additional diffraction-like effects when approximating circular shapes with square cells. Considering acceptable such a difference, we chose the computationally more efficient solution and set the shape of all scatterers as square for both the sensitivity tests and the subsequent inversion. So, with scatterer dimension, we refer to the length of the square side.

As far as the distribution, we chose a completely random distribution of scatterers confined inside the HSZ of the model. As a matter of fact, in real GPR data, no evidence of layering was observed; so, there were no reasons to model any internal layering. Random distribution in fact seemed to be the better solution to realistically model the englacial debris spatial distribution. We here remark that by choosing a totally random distribution, even complex shapes can be produced by the superimposition of multiple square scatterers.

The relation between the scattering occurrence and amplitude as a function to the scatterer dimensions and the wavelength of incident waves can be observed in Figure 3. It can be noted that scattering phenomena occur for dimensions even beyond the threshold of one eighth proposed by Naval et al. (2018). In fact, the simulations showed that the ratio between the dimensions of particles producing the maximum scattering energy and the wavelength of the incident wave is equal to about one fifth. Additional issues arise when using ultra-wide band wavelets containing a large range of frequencies (and so of wavelengths) as in the common GPR equipment. In fact, each spectral component can produce scattering with different energies, making it difficult to estimate the global effect. However, considering the central frequency as a representative of the wavelet is a good enough approximation for many practical applications (Jol, 2009).

Considering incident EM waves with central frequencies equal to 100, 150, 250, 350 and 500 MHz, the corresponding wavelengths, in relation to the ice EM velocity of 0.17 m/ns, are 1.70, 1.10, 0.68, 0.48 and 0.34 m, respectively. From Table 1, the maximum
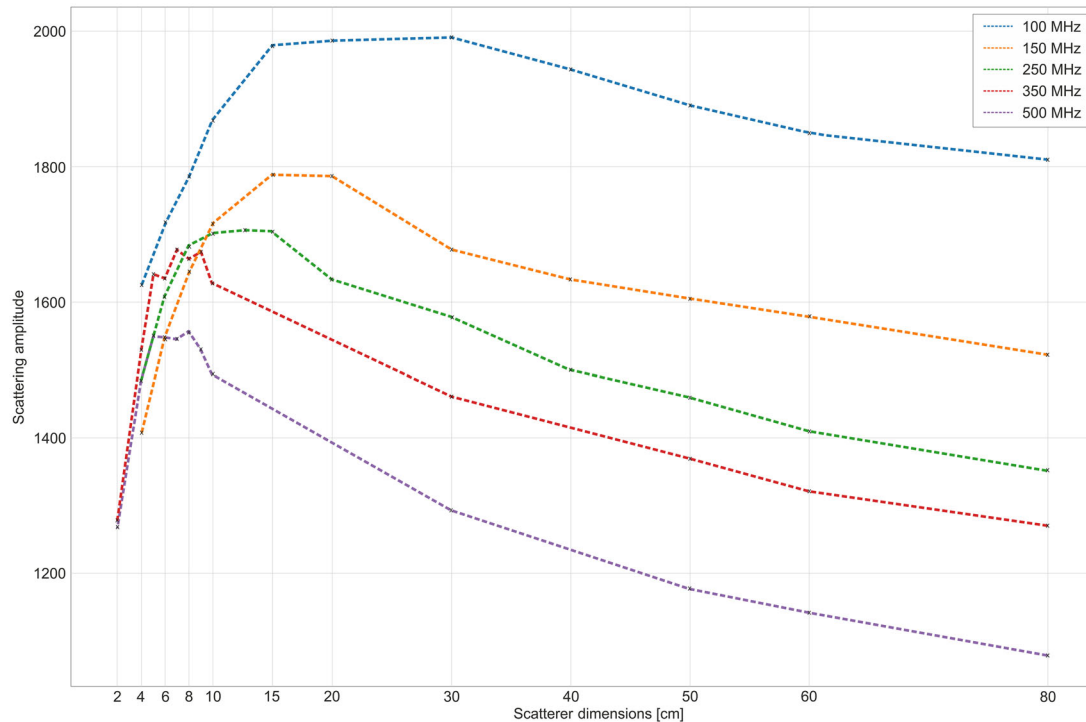
**FIGURE 3** Plot of simulated scattering amplitudes as a function of scatterer dimensions, calculated for different central frequencies between 100 and 500 MHz. All frequencies show a similar trend, with the maximum scattering amplitude shifted to higher scatterer dimensions as the frequency decreases.

**TABLE 1** Relationship between antenna central frequencies and the corresponding wavelengths for a constant electromagnetic (EM) velocity equal to 0.17 m/ns.

| Frequency [MHz] | Wavelength [m] | Dims [m] for max scattering | Wavelength/dims |
|---|---|---|---|
| 100 | 1.70 | 0.34 | 5.00 |
| 150 | 1.10 | 0.20 | 5.50 |
| 250 | 0.68 | 0.13 | 5.23 |
| 350 | 0.48 | 0.09 | 5.33 |
| 500 | 0.34 | 0.07 | 4.85 |

*Note*: Dimensions corresponding to the maximum scattering amplitude are referred to Figure 3. The ratios between wavelengths and dimensions producing maximum scattering amplitude are almost equal to five for all the cases.

scattering energy is caused by scatterer dimensions of 0.34, 0.20, 0.13, 0.09 and 0.07 m, respectively, resulting in a dimension-to-wavelength ratio equal to about one fifth in all the cases. This analysis allowed us to determine the dimension corresponding to the maximum scattering energy and, consequently, to the minimum rock fraction able to create the highest scattering. In addition, it allowed us to narrow down the range of scatterer dimension during the inversion, which was set from 0.13 m to 0.60 m, where the latter is the theoretical limit between diffraction and reflection.

Dielectric permittivity is one of the parameters describing the macroscopic behaviour of materials to the application of an EM field. In a dielectric medium, as ice without relevant amount of water affecting the propaga-

tion of the EM wave, we could consider the dielectric permittivity as the main parameter describing the EM behaviour of the material (Jol, 2009), being the electric conductivity negligible, at least as first approximation (Evans, 1965). Figure 4a shows that all the trends of the measured scattering energy for increasing $\varepsilon_r$ in relation to different scatterer dimensions exhibit a steep increase for size up to about 0.10 m and then a mild decrease and a stabilization for dimensions larger than about 0.60 m. For increasing $\varepsilon_r$, from 5 to 9, the total energy almost doubles its maximum value (Figure 4a). Considering the low dielectric permittivity value of the ice ($\varepsilon_r = 3.2$), a higher $\varepsilon_r$ of the debris results in a higher contrast of EM impedance between debris and ice, thus highly increasing scattering energy, when all the other parameters
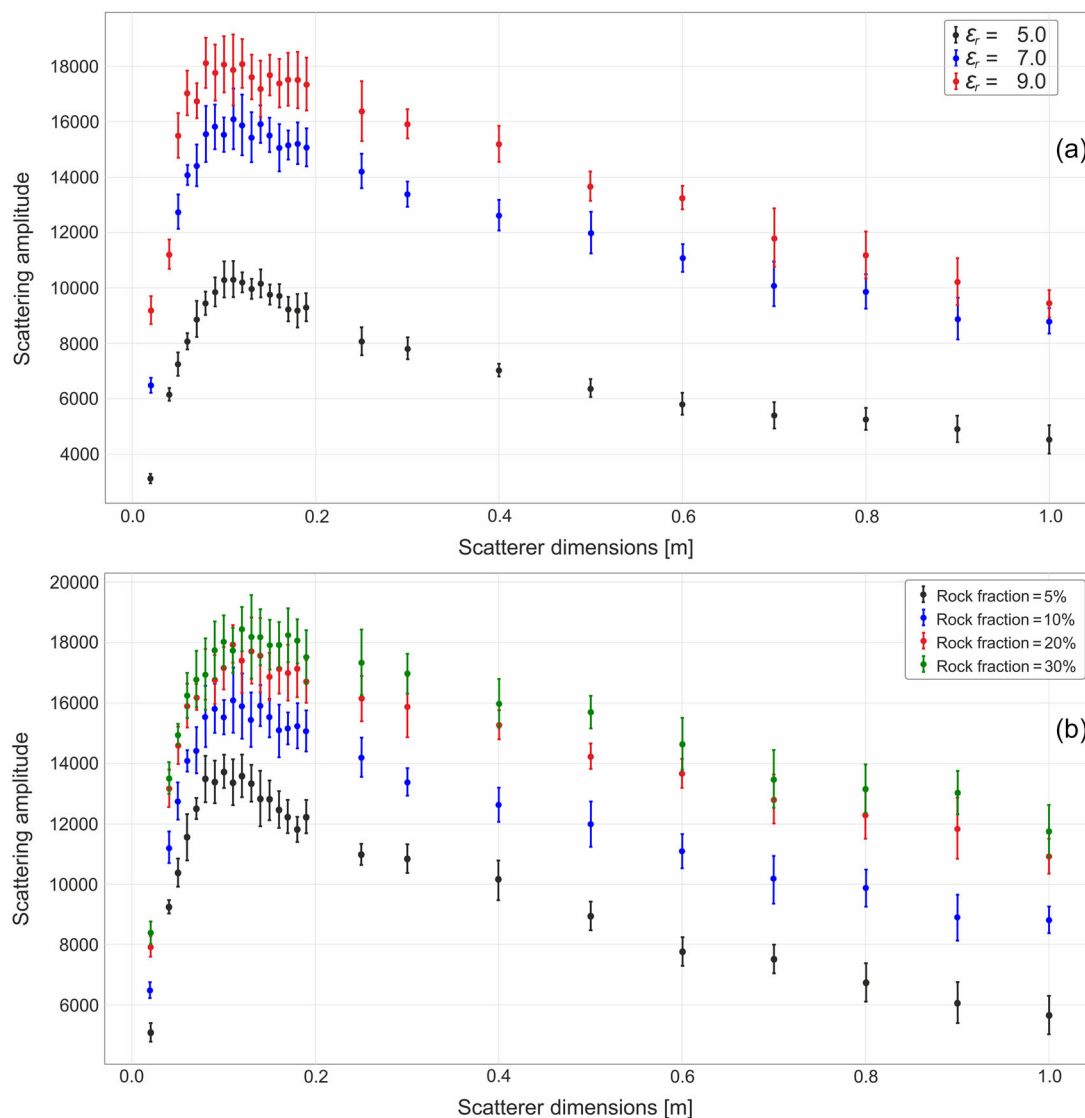
**FIGURE 4** Plots of simulated scattering amplitudes as a function of scatterer dimensions, calculated for different dielectric permittivity $\varepsilon_r$ (a) and different rock fractions (b).

are unchanged. Due to the impossibility of recognizing isolated and undistorted hyperbolic diffractions because of interference phenomena that also often prevent an affordable velocity estimate, we assumed that the dielectric permittivity of the debris should be equal or close to the $\varepsilon_r$ of the bedrock.

This is quite realistic for the Eastern Gran Zebrù glacier, considering that the current debris concentration at the surface of the Eastern Gran Zebrù glacier is due to the rocky walls laterally bordering the glacier (Tarca & Guglielmin, 2022). It is therefore convenient to approximate the value of the dielectric permittivity of the debris to the value of the source rock/bedrock which is composed by different metamorphic rocks, including gneiss and schists. From the new analysis of hyperbolic diffractions, a mean value of $\varepsilon_r = 7$ was set for the inversion.

According to Forte et al. (2021), the most probable hypothesis explaining the high concentration of debris inside a glacier is a negative mass balance period during which a glacier retreated and debris from the lateral rocky walls concentrated over the glacier surface (see, Figure S1). The debris is subsequently incorporated into the ice through crevasses and/or moulins, and the residual ice becomes a mixture of ice and debris, as currently imaged, for example, in the Eastern Gran Zebrù dataset (Forte et al., 2021).

Regarding the rock fraction, it is more rational to consider the volumetric ratio between ice and scatterers instead of the absolute number of scatterers. A higher rock fraction corresponds to a higher scattering amplitude, the variation of which in Figure 4b has a similar trend to the previously reported tests for both $\varepsilon_r$ and the central frequency. All maximum scattering amplitudes

for increasing rock fractions concentrate on scatterer dimensions of about 0.10 m, with a steep decrease for lower dimensions and a moderate decrease for higher dimensions. The behaviour at high dimensions can be explained as scattering is no longer the dominant phenomenon anymore, moving, as expected, from pure scattering to reflections when the dimensions of the scatterers reach and exceed values around the dominant wavelength of the input wavelet.

Results of sensitivity tests allowed us to simplify the subsequent inversion focusing on the two crucial parameters affecting the scattering energy and occurrence, namely the scatterer dimension and the rock fraction.

## Use of Trend as target function

*Trend* calculation starts after the arrival of direct waves (air/ground), which are not used to solve the inverse problem. Figure 5 shows the *Trends* of three synthetic models characterized by fixed scatterer dimensions of 0.13 m (Figure 5a–d) and 0.02 m (Figure 5a′–d′) and rock fractions equal to 1%, 10% and 50%.

It is interesting to notice that when scatterer dimension becomes larger (0.13 m in Figure 5a), the reflector is visible only for small rock fractions (blue line in Figure 5a), whereas the reflector is always apparent for small scatterer dimension (Figure 5a′), even for high rock fractions (green line in Figure 5a′). In addition, the *Trend* shows a high peak at about 130–150 ns, corresponding to the boundary between clean ice and HSZ, with rock fractions of 10% and 50% only when quite large scatterer dimensions are simulated (Figure 5a). For smaller dimensions, the *Trend* has a more constant value and lower overall amplitude (Figure 5a′). The HSZ-bedrock reflector is visible only in specific situations. While in Figure 5a it can be hardly imaged only for rock fractions close to 1%, when the scatterer dimension is close to 2 cm it is always apparent (Figure 5a′), even when the rock fraction reaches 50%. For increasing rock fractions, a remarkable shift towards higher times occurs, being the whole EM velocity lower, as expected for ice ($v \sim 0.17$ m/ns) with higher rock fractions ($v \sim 0.11$ m/ns in the present case). Considering higher scatterer dimension, equal to 0.26 m and 0.39 m (Figures S2 and S3), a similar behaviour is found, confirming the previous outcomes.

## Scattering inversion

The analysis of the scattering energy in relation to the central frequency of the GPR signal, described in Figure 3, allowed us to define the scatterer dimension causing the highest scattering energy, corresponding to one fifth of the wavelength, as previously highlighted. For a 250 MHz antenna, as the one used in the acquisition

of the Eastern Gran Zebrù dataset, it turned out to be equal to 0.13 m. Therefore, we performed the first inversion of real data considering a constant 0.13 m size of the scatterers. With this assumption, a 2.5% rock fraction generates a scattering *Trend* comparable to the real data (Figure 6a,a′). Overall, 2.5% is thus the minimum rock fraction for scatterers of constant size able to generate a scattering amplitude *Trend* mimicking the field data. So, it is possible to give a rough estimate of the rock fraction by assuming the debris dimensions are all equal to one fifth of the wavelength, and consequently determining the minimum possible rock fraction generating the HSZ. Inversion tests were further performed considering constant scatterer size of 0.26, 0.39 and 0.60 m to evaluate the behaviour of the *Trend* as a function of the increasing size of the scatterers. Figure 6a–d shows the *Trend* of field data (black lines), the computed *Trend* closest to the field one (referred to as the winner *Trend*, green lines) and all the computed *Trends* resulting from simulations (10 for each rock fraction) for different rock fractions all performed on models with scatterers of constant size. Figure 6a′–d′ displays the mean square error (MSE) functions between field and synthetic data *Trends* used to estimate the rock fractions of field data considering different fixed dimension scatterers (equal to 0.13, 0.26, 0.39, 0.60 m).

As expected, with the increase of the scatterer dimension, the corresponding estimated rock fraction increases from 2.5% of the 0.13 m model, to 9%, of the 0.60 m model when minimizing the difference between the synthetic and the field data *Trends*. The difference between the synthetic and field *Trends*, in terms of MSE, has an order of magnitude equal for all the inversions, suggesting the stability of the methodology, reaching the lowest value for the 0.13 m model. The shape of the MSE function defines a quite sharp minimum value corresponding to the rock fraction generating the HSZ for the 0.13 m model, widening as the scatterer dimension increases (Figure 6a′–d′). Such behaviour of the MSE function highlights the robustness of the methodology, especially for smaller scatterer dimension: The MSE function for the 0.13 m model is very sensitive even to small variations in rock fraction; therefore, we can easily identify a very narrow minimum. For larger scattering dimensions, the minimum is less defined but still clearly recognizable. This could be due to different factors: first, the fact that for 0.60 m with very small rock fractions, we are introducing just very few scatterers, leading the methodology to be less randomized and more model-dependent. In fact, if we assume the area of the model is equal to 15 m × 20 m and a scatterer dimension of 0.60 m, we can easily compute how many blocks we should introduce to get a 5% rock fraction, that is just 42 individual scatterers. In addition, as we are very close to reflection behaviour, this can lead us to an unstable solution, as, in this case, the position of the scatterers is predominant in the result.
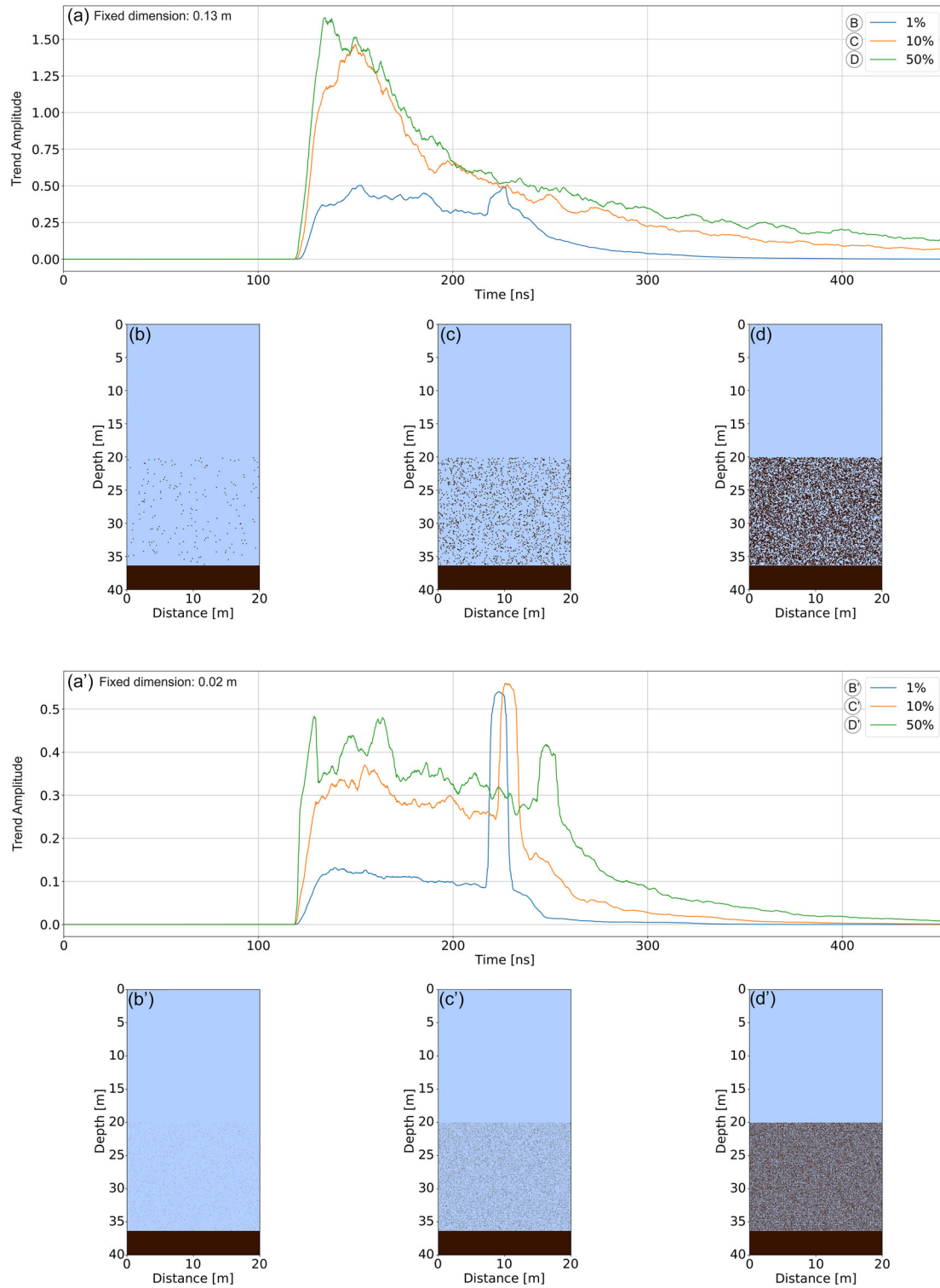
**FIGURE 5** Comparison of *Trends* for constant scatterer dimension equal to 0.13 m (A) and 0.02 m (A′) and different rock fractions, respectively, equal to 1% (B and B′), 10% (C and C′) and 50% (D and D′), all with random spatial distribution. Air and ground waves are not modelled. See text for details.
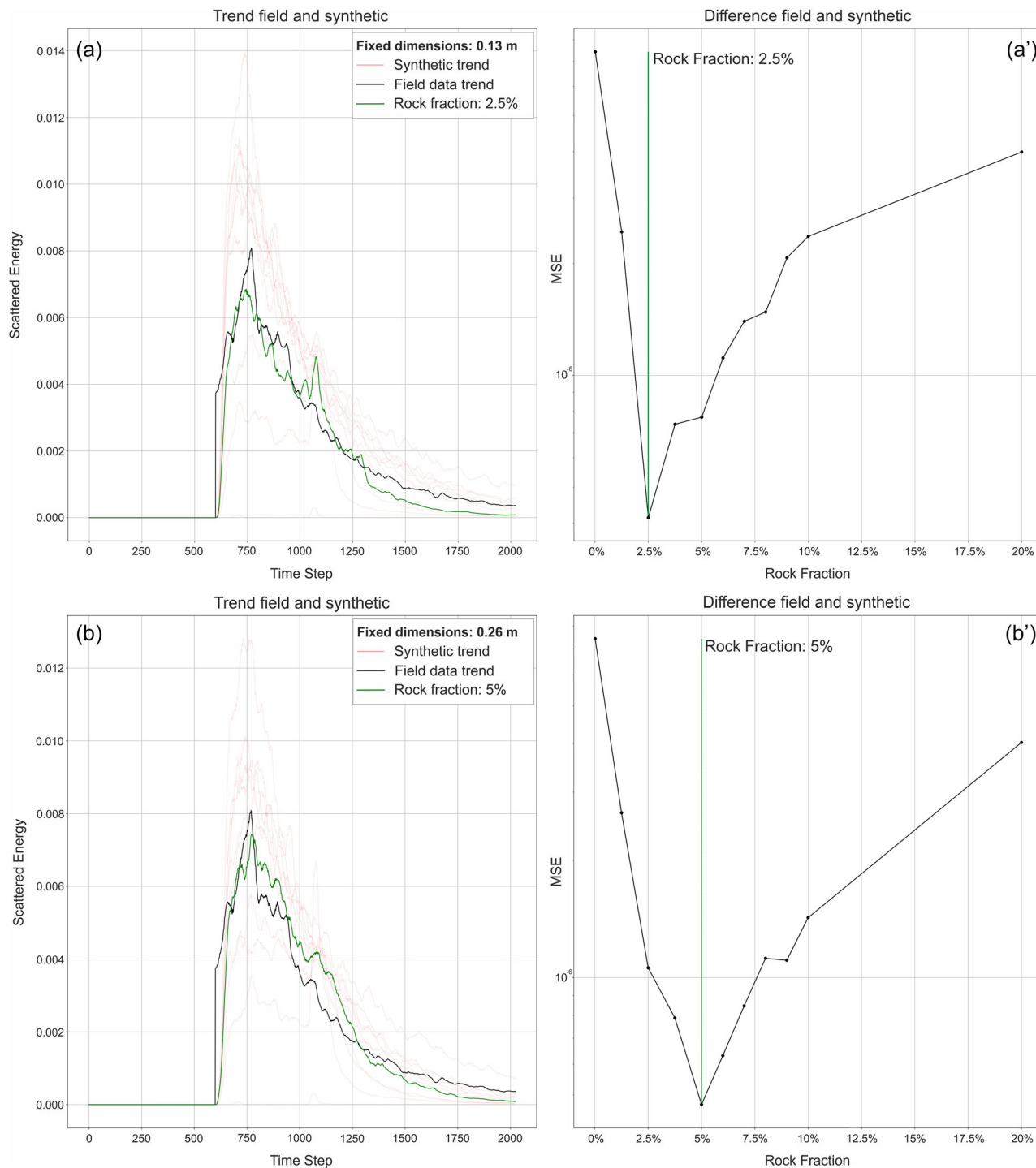
**FIGURE 6** Inversions performed with a fixed size of the scatterer equal to 0.13 m (a and a′), 0.26 m (b and b′), 0.39 m (c and c′) and 0.60 m (d and d′). Parts (a)–(d) present the comparison of the *Trend* of real data (in black) and the winner *Trend* (in green), resulting from all simulations with different rock fraction values performed with the fixed size of the scatterers (in pale red). Parts (a′)–(d′) show the mean square error (MSE) functions (in black) and in green the rock fraction which minimizes the MSE between real and synthetic data.

For intermediate dimensions (0.26 m and 0.39 m), although the MSE function sharpness is more pronounced for the 0.26 m model, the rock fraction necessary to generate scattering is almost the same, equal to about 5% in both cases (Figure 6b′,c′).

Up to this point, all inversions were performed considering a purely theoretical setting with all scatterers having the same dimension. However, such a setting is not representative of a natural glacial environment. We therefore modelled a more realistic situation by uniformly
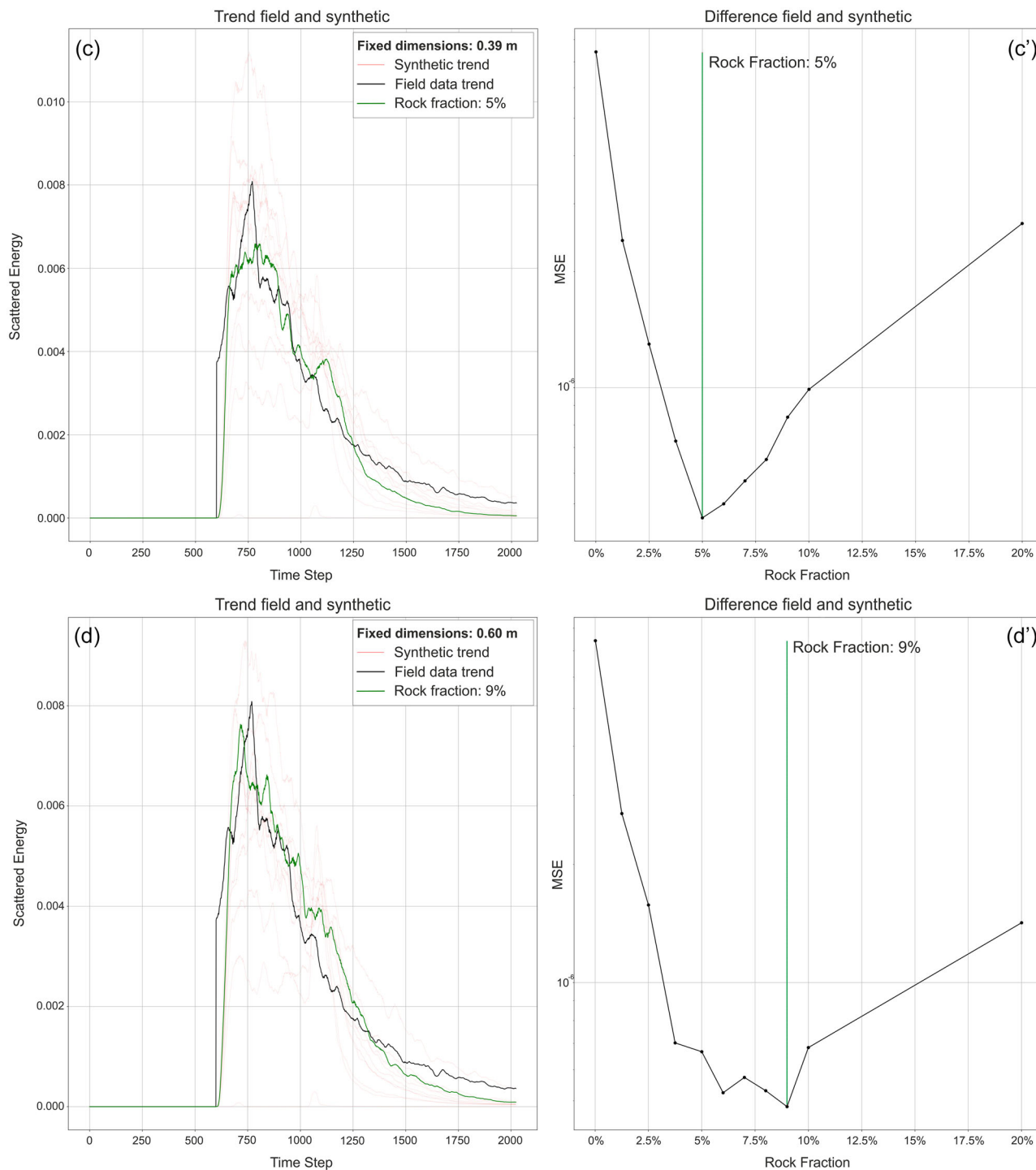
**FIGURE 6** Continued

randomizing the scatterer dimensions within a specific range, equal in the present case to 0.13–0.60 m, referred hereafter to the *mixed model*. With this setting, we estimated a rock fraction equal to 6.5% (Figure 7) for the analysed real dataset. The randomization of the scatterer size between 0.13 m and 0.60 m affects the shape of the MSE function, which does not show an evident minimum as in the previous cases.

The stability of the proposed methodology was further validated by selecting a different set of field data to perform the inversion. Such a set of field data is located in a different region (at about 400 m of distance and 90 m higher in elevation) of the same glacier also characterized by clean ice above the HSZ, which appears quite similar from an amplitude point of view to the previous analysed field data. Results confirmed a rock fraction
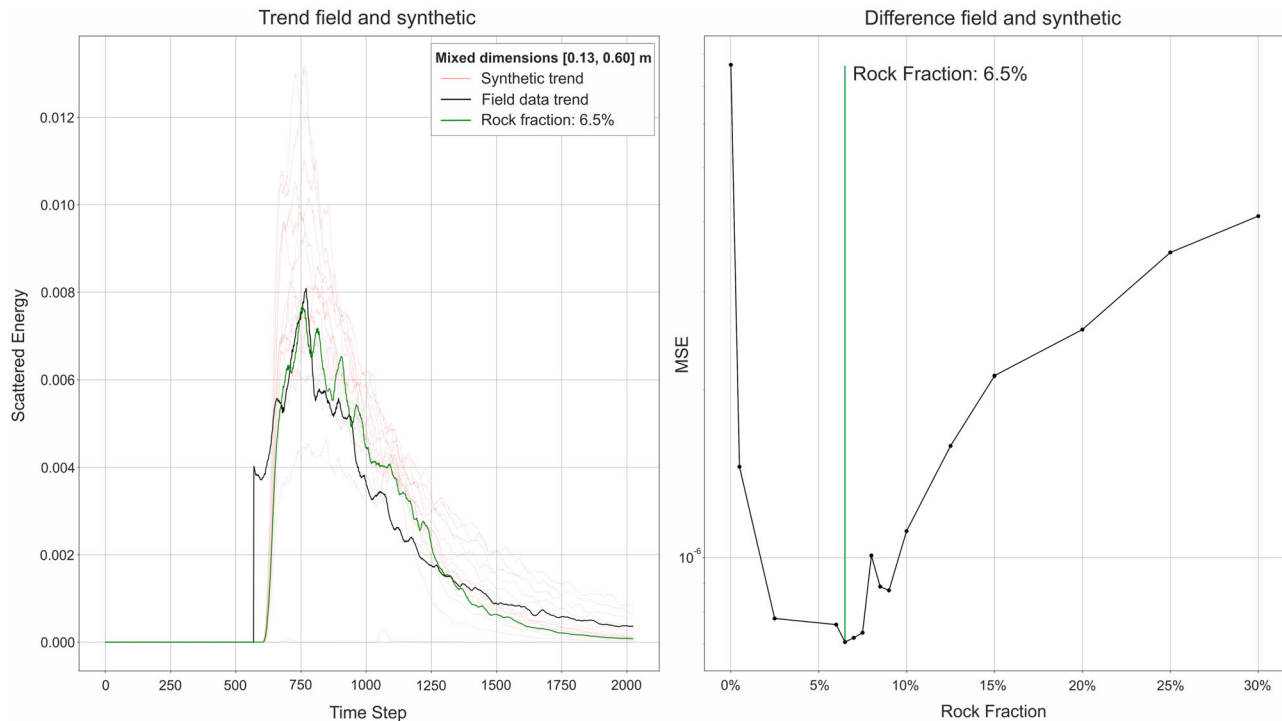
**FIGURE 7**   Inversions performed on a mixed-dimension model [0.13–0.60] m. On the left: the *Trend* of real data is shown in black, the *Trend* closest to the real data in green and all the computed *Trends* resulting from all simulations for different rock fraction values performed with the mixed model in pale red. On the right: the mean square error (MSE) between real and synthetic data used to evaluate the best rock fraction for the inversion is shown in black.

likely below 10% for a random mixed model (see, Figure S4).

## Assumptions and limitations

Modelling a real situation needs to consider some base assumptions in order to reduce the complexity of the problem. The first one is the dimension of the cell model, which causes the choice of model resolution. Its dimension has implications on the representation of the waveform and the returned signal.

The main limitation in exploiting *gprMax* is the large computational costs and memory requirements in the case of 3-D simulations and when a high resolution of the spatial grid is mandatory. In our study, we needed to perform at least 10 simulations for each inversion step in order to assess the stability and robustness of the assumptions we made. The performed inversions are computationally demanding: The random model generation can get to not negligible computational times when small scatterers have to be modelled (like in the 0.02-m case).

In addition, in order to guarantee a good randomness of the model, we performed 10 simulations for each model for each rock fraction. If we consider the results shown in Figure 7, we need to perform 160 numerical simulations with a mean of 2 min each. This requires

about 5 h per inverted profile on a server with an NVIDIA GRID A100D 20 GB, a 32-core processor and 128 GB Ram.

Another evident limitation of our model is that we tried to model a 3-D situation by running a 2-D simulation, in order to simplify the whole procedure and reduce the computational costs. Obviously, we do not consider out-of-plane energy in the simulation, as well as scatterers with 3-D irregular shapes.

However, the assumption of randomness of debris distribution allowed to take into account in our methodology also secondary scattering events and interference phenomena similar to the ones occurring also in a natural setting. As a matter of fact, as we exploited *gprMax* finite-difference algorithm, it takes into account the occurrence of multiple scattering in the case of overlapping debris particles, in opposition to the method recently proposed by Hunziker et al. (2023), where a crucial assumption is that debris particles are far enough from each other. In *gprMax* simulations, when a debris particle partially overlaps another (ore even more than one) complex debris shapes are created making the model somehow more similar to a real situation, whereas the previously set rock fraction is slightly decreased.

As far as the electrical conductivity, we did not consider it as one of the main parameters in the inversion

process. We simulated different scenarios for both null conductivity and for scatterer conductivity having different values, but in all the cases, the results are quite similar with amplitudes only slightly decreasing for higher conductivities (Figure S5). It is certainly true that the electrical conductivity of rocks can vary over a wide range; however, we considered that when geologic materials are frozen and virtually no free water is present, the overall conductivity decreases and its range is indeed smaller. In any case, we considered the electrical permittivity as the main parameter responsible for scattering, whereas, as stated, the electrical conductivity variations are considered less important, at least as a first approximation. In order to justify this assumption, we provide in Figure S5 a sensitivity test focused on the electrical conductivity of the scatterers, keeping all the other parameters constant. We set the conductivity of debris equal to 0, 1 and 10 mS/m (while always keeping the conductivity of ice null). Results (Figure S5D) demonstrated that no significant variations are produced, even if with null conductivity a slightly higher (about 15%–20%) mean scattering amplitude is obtained. When the amount of scatterers is similar (or even higher) than the ice, that is there is a debris (frozen) layer over or in between the ice, the effect of attenuation due to conductivity increases because the bulk attenuation of the investigated volume increases (Franke et al., 2023; Hunziker et al., 2023).

Moreover, englacial attenuation can certainly occur, specifically in situations where not a negligible amount of free water is present, contributing to a decrease in the overall amplitude of the signal; however, in our simplified model, we did not consider such an effect.

The range of scatterer dimension is surely a crucial parameter. In a natural glacial environment, the range of debris size is typically very large often encompassing sediments from boulders to blocks, sand, silt and even clay (Anderson & Anderson, 2016). Significant scattering cannot occur due to very small particles (i.e., sensibly smaller than one eighth of the wavelength corresponding to the dominant frequency of the GPR signal), but aggregated sediments forming pockets or lenses can surely contribute, which is not considered in our modelling. However, we made tests even for small scatterer dimension and found that the effects in terms of amplitude (or of *Trend* function) are sensibly smaller than for sizes closer to one fifth of the dominant wavelength of the exploited signal. For instance, in Figure 5a′ where the results of fixed 0.02 m scatterers are simulated the *Trend* function reaches maximum values lower than one third of the ones obtained for 0.13 m (Figure 5a) for all the simulated rock fractions. When independent information about the debris size and distribution are available, they can be included to better constrain the inversion procedure.

The assumption to have clean ice over the HSZ is not always realistic, for example when there is layered firn, a snow cover, or internal glacial features like crevasses or moulins, or even debris layers, which strongly affect the propagation of the EM signal (Franke et al., 2023). Further work should be addressed towards the introduction of fractal boxes (Giannakis et al., 2016; Peplinski et al., 1995) to model surface anisotropy and additional tests could be performed also to evaluate the effect of liquid water and further investigate the heterogeneity of the debris. In addition, training a neural network (NN) to predict the *Trend* starting from a limited number of parameters could reduce the computational load of the whole approach (Akhaury et al., 2021; Giannakis et al., 2021; Roncoroni et al., 2021). This would open new perspectives for this type of inversions like a fully automatic procedure based on the NN and on a gradient descent operator that could substantially reduce both time and computational costs, possibly without decreasing the overall efficiency of the proposed procedure.

In addition, estimates on the debris content could be implemented/adapted even in different glaciological conditions, like for instance ice sheets in which englacial debris is sometimes detected (e.g. Winter et al., 2019) or in debris-covered glaciers, rock glaciers or dead ice patches, for which it is essential to estimate the ice to debris ratio in order to realistically quantify the total stored water amount, in turn essential for affordable evolution forecasts (Santin et al., 2023).

## CONCLUSIONS

We propose a workflow to estimate the debris content within ice by exploiting the diffuse scattering, which is often recorded in some portions of real GPR datasets collected on various glaciers. The proposed method, even when specific information on the grain size is not available, can estimate the order of magnitude of the rock fraction percentage, within a small enough range. Moreover, the minimum quantity of debris can be estimated as it corresponds to a model with fixed grain size equal to one fifth of the dominant wavelength of the used GPR signal. When additional information is available about scatterer dimensions, characteristics and EM properties, it can be easily included to constrain the inversion process. The results obtained from the case study demonstrate that the methodology is very robust and stable, as well as the use of *Trend* function allowed to give robust results for the inversion process. The method obviously has some restrictions and limitations, which have been detailed discussed and addressed in a dedicated section. We concluded that a rock fraction even below 10% can be responsible for HSZs imaged in GPR glaciological datasets.

## CONFLICT OF INTEREST

On behalf of all the authors, the corresponding author (IS) declares that no conflict exists for all authors for the publication of this paper.

## DATA AVAILABILITY STATEMENT

GPR data and Python codes related to this study can be found at https://github.com/Giacomo-Roncoroni/HSZ.

## ORCID

*Ilaria Santin* https://orcid.org/0000-0003-3566-2189
*Giacomo Roncoroni* https://orcid.org/0000-0003-0893-6674
*Emanuele Forte* https://orcid.org/0000-0002-5995-9254
*Michele Pipan* https://orcid.org/0000-0003-3095-6305

## REFERENCES

Anderson, L.S. & Anderson, R.S. (2016) Modelling debris-covered glaciers: response to steady debris deposition. *The Cryosphere*, 10, 1105–1124. https://doi.org/10.5194/tc-10-1105-2016

Akhaury, U., Giannakis, I., Warren, C. & Giannopoulos, A. (2021) Machine learning based forward solver: an automatic framework in gprMax. In: *Proceedings of 11th International Workshop on Advanced Ground Penetrating Radar (IWAGPR), Valletta, Malta*. Piscataway, NJ, IEEE. pp. 1–6. https://doi.org/10.1109/IWAGPR50767.2021.9843172

Bano, M. (2006) Modeling GPR reflection from a water table. Why high GPR frequency don't image the water table? In: *Proceedings of the EAGE 68th Conference & Exhibition, Vienna, Austria*.

Barto, A.G. & Mahadevan, S. (2003) Recent advances in hierarchical reinforcement learning. *Discrete Event Dynamic Systems*, 13, 341–379. https://doi.org/10.1023/A:1025696116075

Bradford, J.H., Nichols, J., Mikesell, T. & Harper, J. (2009) Continuous profiles of electromagnetic wave velocity and water content in glaciers: an example from Bench Glacier, Alaska, USA. *Annales of Glaciology*, 50(51), 1–9. https://doi.org/10.3189/172756409789097540

Cheng, W., Sun, H.-H., Tan, K.H. & Fan, Z. (2023) Estimating the diameter of reinforcing bars using an ultra-wideband MIMO GPR array. *Construction and Building Materials*, 365, 129924. https://doi.org/10.1016/j.conbuildmat.2022.129924

Colombero, C., Comina, C., De Toma, E., Franco, D. & Godio, A. (2019) Ice thickness estimation from geophysical investigations on the terminal lobes of Belvedere Glacier (NW Italian Alps). *Remote Sensing*, 11, 805. https://doi.org/10.3390/rs11070805

Delf, R., Bingham, R.G., Curtis, A., Singh, S., Giannopoulos, A., Schwarz, B. et al. (2022) Reanalysis of polythermal glacier thermal structure using radar diffraction focusing. *Journal of Geophysical Research – Earth Science*, 127, 2. https://doi.org/10.1029/2021JF006382

Diamanti, N. & Annan, A.P. (2019) Understanding the use of ground-penetrating radar for assessing clandestine tunnel detection. *The Leading Edge*, 38, 453–459. https://doi.org/10.1190/tle38060453.1

Diamanti, N., Annan, A.P. & Vargemezis, G. (2022) Phantom subsurface targets in ground penetrating radar (GPR) data. *Geophysics*, 87, 4. https://doi.org/10.1190/geo2021-0692.1

Dossi, M., Forte, E. & Pipan, M. (2018) Quantitative analysis of GPR signals: transmitted wavelet, amplitude decay and sampling-related amplitude distortions. *Pure and Applied Geophysics*, 175, 1103–1122. https://doi.org/10.1007/s00024-017-1752-2

Evans, S. (1965) Dielectric properties of ice and snow–a review. *Journal of Glaciology*, 5(42), 773–792. https://doi.org/10.3189/S0022143000018840

Feng, J., Yang, L., Hoxha, E., Jiang, B. & Xiao, J. (2023) Robotic inspection of underground utilities for construction survey using a ground penetrating radar. *Journal of Computing in Civil Engineering*, 37(1), 04022049. https://doi.org/10.1061/(ASCE)CP.1943-5487.0001062

Forte, E., Santin, I., Ponti, S., Colucci, R.R., Gutgesell, P. & Guglielmin, M. (2021) New insights in glaciers characterization by differential diagnosis integrating GPR and remote sensing techniques: a case study for the Eastern Gran Zebrù glacier (Central Alps). *Remote Sensing of Environment*, 267, 112715. https://doi.org/10.1016/j.rse.2021.112715

Franke, S., Gerber, T.A., Warren, C., Jansen, D., Eisen, O. & Dahl-Jensen, D. (2023) Investigating the radar response of englacial debris entrained basal ice units in East Antarctica using electromagnetic forward modelling. *IEEE Transactions on Geoscience and Remote Sensing*, 61, 1–16. https://doi.org/10.1109/TGRS.2023.3277874

Giannakis, I., Giannopoulos, A. & Warren, C. (2016) A realistic FDTD numerical modeling framework of ground penetrating radar for landmine detection. *IEEE Journal of Selected Topics in Applied Earth Observation and Remote Sensing*, 9(1), 37–51. https://doi.org/10.1109/JSTARS.2015.2468597

Giannakis, I., Giannopoulos, A. & Warren, C. (2021) A machine learning scheme for estimating the diameter of reinforcing bars using ground penetrating radar. *IEEE Geoscience and Remote Sensing Letters*, 18(3), 461–465. https://doi.org/10.1109/LGRS.2020.2977505

Giannopoulos, A. & Diamanti, N. (2008) Numerical modelling of ground penetrating radar response from rough subsurface interfaces. *Near Surface Geophysics*, 6, 357–369. https://doi.org/10.3997/1873-0604.2008024

González-Huici, M.A. & Giovanneschi, F. (2013) A combined strategy for landmine detection and identification using synthetic GPR responses. *Journal of Applied Geophysics*, 99, 154–165. https://doi.org/10.1016/j.jappgeo.2013.08.006

Haruzi, P., Schmäck, J., Zhou, Z., Kruk, J., Vereecken, H., Vanderborght, J. et al.(2022) Detection of tracer plumes using full-waveform inversion of time-lapse ground penetrating radar data: a numerical study in a high-resolution aquifer model. *Water Resources Research*, 58(5), e2021WR030110. https://doi.org/10.1029/2021WR030110

Hillebrand, T.R., Conway, H., Koutnik, M., Martín, C., Paden, J. & Winberry, J.P. (2021) Radio-echo sounding and waveform modeling reveal abundant marine ice in former rifts and basal crevasses within Crary Ice Rise, Antarctica. *Journal of Glaciology*, 67(264), 641–652. https://doi.org/10.1017/jog.2021.17

Hunziker, J., Slob, E.C. & Irving, J. (2023) Fast 3D ground penetrating radar simulations for glaciers. *Computers & Geosciences*, 173, 105320. https://doi.org/10.1016/j.cageo.2023.105320

Jol, H.M. (2009) *Ground penetrating radar theory and application*, 1st edition. Amsterdam: Elsevier Science.

Kelly, T.B., Angel, M.N., O'Connor, D.E., Huff, C.C., Morris, L.E. & Wach, G.D. (2021) A novel approach to 3D modelling ground-penetrating radar (GPR) data – a case study of a cemetery and

applications for criminal investigation. *Forensic Science International*, 325, 110882. https://doi.org/10.1016/j.forsciint.2021.110882

King, E.C., Smith, A.M., Murray, T. & Stuart, G.W. (2008) Glacier-bed characteristics of midtre lovénbreen, Svalbard, from high-resolution seismic and radar surveying. *Journal of Glaciology*, 54(184), 145–156.

Maisto, D., Donnarumma, F. & Pezzulo, G. (2015) Divide et impera: subgoaling reduces the complexity of probabilistic inference and problem solving. *Journal of The Royal Society Interface*, 12, 1335. https://doi.org/10.1098/rsif.2014.1335

Mie, G. (1908) Beiträge zur Optik trüber Medien, speziell kolloidaler Metallösungen. *Annalen der Physik*, 330(3), 377–445.

Moran, M.L., Greenfield, R.J. & Arcone, S.A. (2003) Modelling GPR radiation and reflection characteristics for a complex temperate glacier bed. *Geophysics*, 68(2), 559–565. https://doi.org/10.1190/1.1567225

Naval, V.S., Santos-Assunçao, S. & Pérez-Gracia, V. (2018) GPR clutter amplitude processing to detect shallow geological targets. *Remote Sensing*, 10, 88. https://doi.org/10.3390/rs10010088

Öztürk, C. & Drahor, M.G. (2010) Synthetic GPR modelling studies on shallow geological properties and its comparison with the real data. In: *Proceedings of the 13th International Conference on Ground Penetrating Radar, Lecce, Italy*. Piscataway, NJ, IEEE. pp. 1—4. https://doi.org/10.1109/ICGPR.2010.5550215

Pajewski, L., Solla, M. & Küçükdemirci, M. (2017) Ground-penetrating radar for archaeology and cultural-heritage diagnostics activities carried out in COST action TU1208. In: *Nondestructive techniques for the assessment and preservation of historic structures*, 1st edition. Boca Raton, FL: CRC Press.

Peplinski, N.R., Ulaby, F.T. & Dobson, M.C. (1995) Dielectric properties of soils in the 0.3–1.3-GHz range. *IEEE Transactions on Geoscience and Remote Sensing*, 33(3), 803–807. https://doi.org/10.1109/36.387598

Pettersson, R., Jansson, P., Huwald, H. & Blatter, H. (2007), Spatial pattern and stability of the cold surface layer of Storglaciären, Sweden. *Journal of Glaciology*, 53(180), 99–109. https://doi.org/10.3189/172756507781833974

Rayleigh, L. (1881) On the electromagnetic theory of light. *The London, Edinburgh, and Dublin Philosophical Magazine and Journal of Science*, 12(73), 81–101. https://doi.org/10.1080/14786448108627074

Reinardy, B.T.I., Booth, A.D., Hughes, A.L.C., Boston, C.M., Åkesson, H., Bakke, J. et al. (2019) Pervasive cold ice within a temperate glacier – implications for glacier thermal regimes, sediment transport and foreland geomorphology. *The Cryosphere*, 13, 827–843. https://doi.org/10.5194/tc-13-827-2019

Roncoroni, G., Fortini, C., Bortolussi, L., Bienati, N. & Pipan, M. (2021) Synthetic seismic data generation with deep learning. *Journal of Applied Geophysics*, 190, 104347. https://doi.org/10.1016/j.jappgeo.2021.104347

Roncoroni, G., Forte, E., Bortolussi, L. & Pipan, M. (2022) Efficient extraction of seismic reflection with deep learning. *Computers & Geosciences*, 166, 105190. https://doi.org/10.1016/j.cageo.2022.105190

Santin, I., Roncoroni, G., Forte, E. & Pipan, M. (2022) GPR inversion and modelling for glacial internal debris estimation and characterization. In: *Proceedings of the 19th International Conference on Ground Penetrating Radar (SEG Global Meeting Abstracts, GPR 2022), 12–17 June 2022, Golden, CO*. Tulsa, OK, SEG. pp. 39–42. https://doi.org/10.1190/gpr2022-064.1

Santin, I., Forte, E., Nicora, M., Ponti, S. & Guglielmin, M. (2023) Where does a glacier end? Integrated geophysical, geomorphological and photogrammetric measurements to image geometry and ice facies distribution. *Catena*, 225, 107016. https://doi.org/10.1016/j.catena.2023.107016

Schennen, S., Wetterich, S., Schirrmeister, L., Schwamborn, G. & Tronicke, J. (2022) Seasonal impact on 3D GPR performance for surveying Yedoma ice complex deposits. *Frontiers in Earth Science*, 10, 741524. https://doi.org/10.3389/feart.2022.741524

Tarca, G. & Guglielmin, M. (2022) Evolution of the sparse debris cover during the ablation season at two small Alpine glaciers (Gran Zebrù and Sforzellina, Ortles-Cevedale group). *Geomorphology*, 409, 108268. https://doi.org/10.1016/j.geomorph.2022.108268

Tsang, L., Kong, J.A. & Ding, K. (2000) *Scattering of electromagnetic waves: theories and applications*. Hoboken, NJ: John Wiley & Sons, Inc.

Warren, C., Giannopoulos, A. & Giannakis, I. (2016) gprMax: open source software to simulate electromagnetic wave propagation for ground penetrating radar. *Computer Physics Communications*, 209, 163–170. https://doi.org/10.1016/j.cpc.2016.08.020

Warren, C., Giannopoulos, A., Gray, A., Giannakis, I., Patterson, A., Wetter, L & Hamrah, A. (2018) A CUDA-based GPU engine for gprMax: open source FDTD electromagnetic simulation software. *Computer Physics Communications*, 237, 208–218. https://doi.org/10.1016/j.cpc.2018.11.007

Winter, K., Woodward, J., Ross, N., Dunning, S.A., Hein, A.S., Westoby, M.J., et al. (2019), Radar-detected englacial debris in the West Antarctic ice sheet. *Geophysical Research Letters*, 46(17–18), 10454–10462. https://doi.org/10.1029/2019gl084012

## SUPPORTING INFORMATION

Additional supporting information can be found online in the Supporting Information section at the end of this article.

---

**How to cite this article:** Santin, I., Roncoroni, G., Forte, E., Gutgesell, P. & Pipan, M. (2024) GPR modelling and inversion to quantify the debris content within ice. *Near Surface Geophysics*, 22, 220–234. https://doi.org/10.1002/nsg.12274